International Journal of Solids and Structures 50 (2013) 310–319

Contents lists available at SciVerse ScienceDirect

International Journal of Solids and Structures

journal homepage: www.elsevier.com/locate/ijsolstr

Instrumented end notched flexure – Crack propagation and process zone monitoring Part II: Data reduction and experimental

M.K. Budzik [a,b,c,d,1], J. Jumel [a,b,c,*], N. Ben Salem [a,b,c,d], M.E.R. Shanahan [a,b,c]

[a] Univ. Bordeaux, I2M, UMR 5295, F-33400 Talence, France
[b] CNRS, I2M, UMR 5295, F-33400 Talence, France
[c] Arts et Metiers ParisTech, I2M, UMR 5295, F-33400 Talence, France
[d] French Space Agency (CNES) – DLA, 75612 Paris Cédex, France

ARTICLE INFO

Article history:
Available online 15 September 2012

Keywords:
End notched flexure
Mode I
Mode II
Process zone
Strain gauges

ABSTRACT

A mode II instrumented end notched flexure three point bending (ENF) adhesion test is described. The adhesive joint consists of two aluminium alloy (AW7075-T6) plates bonded with a structural epoxy adhesive (Hysol® EA 9395™). Strain gauges are attached to the outer surface (backface) of the substrates in the lengthwise direction to measure local surface strain during crack propagation. Simultaneously, load/displacement measurements are performed. Two cases were investigated. The first was static: the joint was loaded below the crack propagation threshold. In the second, applied load above the threshold led to crack propagation. The former test confirmed the predicted load transfer mechanism between bonded and unbonded parts of the joint. In the second case, the crack front process zone was revealed *in situ* in mode II, we believe for the first time. These new results permitted validation of simple or refined analytical/numerical models including those of the cohesive zone. In addition, the backface strain gauge monitoring technique exhibited unexpected mode I contributions, quantitatively evaluated. Finally, *R*-curves are presented, as estimated with various standard models and compared with that postulated, where the process zone is accounted for.

1. Introduction

Adhesively bonded structures are usually designed using either strength or fracture failure criteria (Banea and da Silva, 2009). While strength is relatively easy to evaluate with standard tests on bulk adhesive specimens, there is no consensus on the validity of transposing such data when considering bonded joints. Singular mechanical fields are produced near the edge of bonded specimens which substantially modify the local stress state and lead to crack onset (Erdogan, 1965; He and Hutchinson, 1989). Any structural imperfections in the bondline, such as voids, microcracks, *etc.*, which are inherent in the adhesive joining technique, could produce similar behaviour. Apart from the crack onset problem, it is now commonly, but not unanimously, accepted that the failure of a bonded joint may be described as an unstable crack growth phenomenon amenable to study using linear elastic fracture mechanics formalism. Failure depends on intrinsic parameters of the given system *viz.* fracture energy, G_c, of the bondline, interface(s) and/or substrate(s) (Leguillon, 2002). The double cantilever beam (DCB) test was proposed by the adhesion community to evaluate G_{Ic}, in the case of mode I fracture (Mostovoy et al., 1967). In its classic version, the test piece is composed of two, geometrically and physically similar, beams/plates bonded with an adhesive. The specimen is loaded in opening mode to measure G_{Ic}, as recommended by the (ASTM D3433-99 and D3762-03) standards. Also, mode II (in-plane): G_{IIc}, and mode III (anti-plane): G_{IIIc}, loading have been studied even if considered of less interest since supposed less critical.

Cleavage loading is certainly the most dangerous separation mode for a bonded joint and, in practice, assemblies are designed to sustain shear loads which are associated to the in-plane mode II (Kuczmaszewski, 2006). The strength in such a configuration is evaluated from the popular lap shear joint (LSJ) test (ASTM D3165-07, D2919-01, D3166-99). Although this test was initially intended to evaluate shear *strength*, it is now suggested that this set-up could be treated as a mixed mode, fracture mechanics problem since both peel and shear peak stresses are produced on both sides of the overlap (Goland and Reissner, 1944; Kendall, 1975; Tsai and Morton, 1994). New experimental designs are required for proper evaluation of mode II failure. Using standard DCB specimen geometry, various fixing features and loading configurations have been proposed. Among them, the most frequently used are

* Corresponding author at: Univ. Bordeaux, I2M, UMR 5295, F-33400 Talence, France.
E-mail address: julien.jumel@u-bordeaux1.fr (J. Jumel).
[1] On leave from Technical University of Gdansk, Faculty of Mechanical Engineering, Dept. of Material Engineering and Welding, 80-952 Gdansk, Poland.

0020-7683/$ - see front matter © 2012 Elsevier Ltd. All rights reserved.
http://dx.doi.org/10.1016/j.ijsolstr.2012.08.030

three-point bending end-notched flexure (ENF) (Barrett and Foschi, 1977), four-point bending end-notched flexure (4-ENF) (Martin and Davidson, 1999), end-loaded split (ELS) (Wang and Vu-Khanh, 1996) and tapered end-notched flexure (TENF) (Blackman et al., 2005). Due to the simplicity of the test protocol and sample preparation, the end-notched flexure test is often used. The ASTM task group has conducted a round robin test programme using the ENF specimen as a prelude for the development of an ASTM standard for measuring mode II interlaminar fracture toughness in composites (Mall and Kochar, 1986). This now appears as a draft for a future standard (Davidson and Sun, 2006; ASTM WK22949). In the three point bending configuration, the joint is simply supported by two rollers and loaded in the middle of the span by a third one. The specimen is partially cracked (or initially unbonded) with the crack tip being located between a side and the mid-span roller. If symmetric specimens are considered, pure mode II is expected at (de Moura et al., 2009). Nevertheless, a major inconvenience of the ENF test is that the crack progresses towards the maximal bending moment (under the mid-span) so that the test is unstable (Carlsson et al., 1986). Indeed, the three point bending ENF test is only conditionally stable, even in the case of a displacement controlled experiment. Carlsson et al. (1986) investigated stability conditions in the case of a rigid adhesive layer and found that 'stable' crack growth occurs when the initial crack length (a_0) is larger than a critical value, $a_{0c} \approx 0.35\ L$ ($2L$ = span). A similar formula was proposed by Chai and Mall (1988) when the load is not applied at the mid-span. In the work of Mall and Kochar (1986), the effect of friction between the interfaces was also analysed, using a finite element method. The authors conclude that the frictional effect is negligible when the crack length is greater than a quarter of the span.

Many analytical and numerical analyses have been proposed for finer evaluation of fracture energy. Current practices exploit only macroscopic quantities, such as applied force and imposed displacement, to derive crack position and fracture energy. Data reduction methods are based on simple beam theory (SBT) models, which have been progressively improved by the use of correction coefficients calculated from finer analysis and/or numerical methods. Today, these fracture mechanics tests are also used as a reference for the identification of complex interface models. Alfredsson (2004), Corleto and Hogan (1995) and Ouyang and Li (2009) compared the response of fracture specimens in the case of an interface having elastic, elastic–plastic or nonlinear behaviour. However, the macroscopic, experimental data remain too poor for reliable identification of the complex interface model (Alfano, 2006). More local crack tip opening measurements with J based approach analysis have been proposed for cohesive zone model (CZM) identification (Sørensen and Jacobsen, 2003).

The instrumented beam technique is a complementary method to investigate the cohesive force distribution along the process zone. This protocol has been introduced for mode I and mode III fracture tests (Budzik et al., 2011a,b; Jumel et al., 2011). It consists of attaching a series of resistive strain gauges along the substrates to infer the local cohesive force with these distributed 'load cells'. This also improves the monitoring of crack propagation during the test.

In this paper, the existing methods for analysing ENF three point bending are applied to a mode II fracture test on aluminium specimens bonded with a structural epoxy adhesive. Application of the backface strain monitoring technique (Zhang et al., 1995) to the ENF specimen is also presented. First, simple beam and corrected beam theories are used to evaluate crack propagation kinetics and energy release rate. These results are compared with those obtained from measurements of shear displacement at the edge of the sample, as found with a digital image correlation technique. Finally, the Timoshenko beam on elastic Pasternak type foundation model (two-parameter elastic interface), whose derivation is presented in detail elsewhere (Jumel et al., 2012), is used for finer analysis of the process zone in the vicinity of the crack front, and to improve the evaluation of fracture energy. Theoretical results are in good agreement with experimental data.

This methodology demonstrates its value for refined experimental investigation of cohesive forces in the ENF specimen during fracture tests. The new technique proposed should allow better identification of theoretical interface models such as CZM, based on enriched experimental data.

2. Experimental

2.1. Materials

The end notched flexure test pieces consist of two aluminium alloys plates bonded with a structural epoxy adhesive. Aluminium alloy (Al–Zn) AW7075 – T6 plates were 5 mm thick (t), 25 mm wide (w) and 210 mm long. The Young's modulus of the plates, as evaluated from three point bending was 70 ± 3 GPa. Before bonding, plates were grit blasted using 320 μm (average diameter) SiC particles and subsequently cleaned in an ultrasonic bath (35 kHz) in ethanol for 15 min. Plates were bonded with an epoxy-based adhesive, Hysol® EA 9395™ supplied by Henkel (Henkel Corporation Aerospace Group, Bay Point, CA 94565 USA). The curing agent for this adhesive is based on tetraethylenepentamine (TEPA). As recommended in the supplier's documentation, a 100:17 mixing weight ratio (resin-to-crosslinker) was used for preparation of the adhesive. Both components were hand-mixed with a spatula until a homogeneous aspect was obtained. Substrates were bonded along 160 mm. Two pieces of 1 mm diameter steel wire were inserted between the plates of the specimen, one at each end, in order to obtain constant bondline thickness. A similar configuration was used by Leffler et al. (2007). The distance between the wires was 180 mm, which also corresponds to support span. Curing was performed for one day at 23 °C under 10 bars pressure, and subsequently for 90 min at 66 °C without additional pressure, subsequent cooling being in the oven. A 1 mm thick (t_a) homogeneous bondline was obtained, as controlled with an optical microscope. The adhesive Young's modulus (E_a) was evaluated using a dynamic-mechanical analyser (Metravib + 150, 01 dB-Metravib, Limonest, France) to test dumbbell adhesive specimens of 12 mm gauge length (experimental conditions: 1 Hz, 5 μm dynamic displacement). At ambient temperature, E_a was found to be 4 ± 0.2 GPa.

Three ENF test samples were prepared and tested to evaluate the reproducibility of the results in terms of force–displacement curves. One specimen was fully instrumented with strain gauges.

2.2. End notched flexure (ENF) test

A schematic representation of the ENF test is shown in Fig. 1.

In the standard test configuration, evaluation of fracture data is based on global force–displacement measurements. The ENF sample was loaded with a force, P, normal to the bondline, applied at

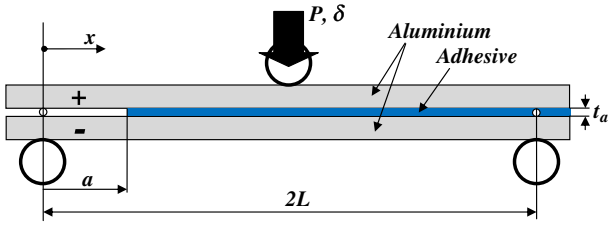

Fig. 1. Schematic representation of the joint geometry and test principle.

the mid-span position, under constant traverse displacement conditions, $d\delta/dt = 0.1$ mm/min, where δ is displacement in z direction. Force was measured with a 10 kN load cell (ZWICK GmbH & Co, Germany). Vertical displacement was measured with a LVDT sensor having a 25 mm range (RDP Electronics Ltd., Wolverhampton, UK) placed under the specimen at the position where load was applied. The distance between the supports, or span ($2L$), was 180 mm. Initial crack length, $a_0 = 44$ mm was obtained after bonding. At first, strains were measured in the 'static' configuration, loaded below the crack propagation load threshold. The joint was loaded up to 400 N and immediately released so that no crack propagation was observed. In the second configuration, referred to as 'fracture', the joint was loaded continuously until fracture initiated followed by 'stable' propagation. When the crack tip reached the mid-span position, a load increase was observed and the test was stopped. In order to create a 'natural' sharp crack, the specimen was initially partially fractured by inserting a steel wedge between the two substrates held with a vice. The observed natural crack length was *ca.* 52 mm (observed from the specimen side view perspective).

2.3. Strain measurements

With strain gauge instrumentation, the substrates are converted effectively into local load cells. This allows for refined investigation of the cohesive force distribution along the bonded substrates and helps in understanding the process zone development and crack propagation mechanism. Fifteen gauges were bonded onto the assembled substrates: 10 at the top and 5 at the bottom. The 10 upper gauges were used for static experiments. In the fracture experiments 5 lower and 5 corresponding upper gauges were used. (This restriction was due to the availability of only 10 channels on the Wheatstone bridge recording apparatus.) Two mm grid gauges of 120 Ω resistance were used (Vishay Precision Group, Raleigh, USA). Ten gauges were bonded in the lengthwise direction along the upper substrate corresponding to the positions: 27, 35, 43, 52, 60, 68, 75, 83, 110, 126 mm, measured from x origin (see Fig. 1). To evaluate strain distribution along both the upper and lower adherends two 'static' load sequences were used. The specimen was first loaded up to 400 N and unloaded, then subsequently, reversed (top to bottom) and loaded and unloaded once more. In other words, the adherends changed successively from compression to tension and *vice versa*. Since 400 N load is well below the fracture onset level, it was assumed that these first tests did not damage the adhesive.

In the 'fracture' mode, the five gauges, top and bottom, were placed at x values of: 52, 60, 68, 75, 83 mm.

2.4. Shear compliance evaluation

During end notched flexure, the bondline is loaded in shear so that the shear compliance evolution (Alfredsson, 2004; Yoshihara, 2005) gives much information: relative slip between both adherends should be detected. In order to observe this, we monitored the free edges of the cracked side of the specimen with a digital video microscope (Dino-Lite Pro, IS Production S.A., St Genis Pouilly, France). Digital Image Correlation (DIC) was used to measure the relative displacements of the corners of the adherends. These operations were effected on grey scale images (1280 × 1024 pixels – size of one pixel corresponds to 30 μm), acquisition period being 5 s. Analysis was performed using Vic2D software (Correlated Solutions Inc., Columbia, USA).

3. Basic theory

A detailed analysis of three-point bending end notched flexure has been proposed in Jumel et al. (2012). Here, we will focus on the formulae used for experimental data reduction, as well as the parameters which control stress distribution and joint failure at the crack tip.

3.1. Simple beam theory (SBT)

Simple beam theory (SBT) is frequently used to analyse ENF results for a straightforward estimate of the energy release rate from force/displacement diagrams. Assuming infinite rigidity of the adhesive layer, the SBT model yields the following expression for ENF specimen compliance (Russell, 1982):

$$C = \frac{\delta}{P} = \frac{3a_{eff}^3 + 2L^3}{8wt^3E} \tag{1}$$

where δ is the load point displacement and P is the applied force (distributed across the sample width), both measured continuously during the test. A correction has been proposed (Wang and Williams, 1992) to take into account interface compliance. From Eq. (1) an 'effective' crack length, a_{eff}, can be found, which is generally larger than the real 'geometrical' length, a. From expression (1), according to linear elastic fracture mechanics (LEFM), the strain energy release rate, G_{II} is given by Russell (1982):

$$G_{II} = \frac{9a_{eff}^2P^2}{16w^2t^3E} \tag{2}$$

3.2. Timoshenko beam on two-parameter elastic interface

To calculate the deformation of the ENF specimen under three point loading, we propose a model consisting of two Timoshenko beams bonded with a two parameters elastic foundation, detailed in Part I of this project (Jumel et al., 2012). The local equilibrium of each adherend is given by the classic beam equilibrium equations:

$$\frac{dM_i}{dx} + T_i - \frac{t}{2}w\tau = 0 \tag{3}$$

$$\frac{dT_i}{dx} - sw\sigma = 0 \tag{4}$$

$$\frac{dN_i}{dx} - sw\tau = 0 \tag{5}$$

where index $i = \pm$ refers to the upper or lower adherend (see Fig. 1), $s = 1$ for the upper adherend and $s = -1$ for the lower adherend (note that i has the opposite sign from s). M_i, T_i and N_i are respectively the bending moment, shear and the normal beam cohesive forces. σ and τ are peel and shear stresses in the adhesive, and t is the thickness of the beams, which are supposed to have identical geometry and elastic properties. Additional constitutive equations are given by Timoshenko's beam model:

$$M_i = EI\frac{d\varphi_i}{dx} \tag{6}$$

$$T_i = \kappa GS\left[\frac{dv_i}{dx} - \varphi_i\right] \tag{7}$$

$$N_i = ES\frac{du_i}{dx} \tag{8}$$

where E and G are respectively the adherend Young's and shear modulus. $S = wt$ and $I = wt^3/12$ are beam cross sectional area and second moment of area, w is beam width, and φ, v and u are respectively beam rotation, deflection and longitudinal displacement. κ is the shear correction coefficient $\approx 5/6$ in the case of rectangular cross section (Reissner, 1944). Here, the behaviour of all materials

is supposed to be linear elastic including that of the bondline, given by the following relations:

$$\sigma = \frac{E_a^*}{t_a}[v_+ - v_-] \tag{9}$$

$$\tau = \frac{G_a}{t_a}\left[\frac{t}{2}[\varphi_+ + \varphi_-] + u_+ - u_-\right] \tag{10}$$

where

$$E_a^* = \frac{E_a(1-\nu_a)}{(1+\nu_a)(1-2\nu_a)} \tag{11}$$

$$G_a = \frac{E_a}{2(1+\nu_a)} \tag{12}$$

and t_a is the elastic layer (adhesive) thickness. E_a and ν_a are respectively Young's modulus and Poisson's ratio of the adhesive.

By combining Eqs. (3)–(10), two differential equations can be obtained which determine the stress distribution along the bondline (Bennati et al., 2009). Complete solution of the differential system is presented in the first part of this work (Jumel et al., 2012). The main conclusion is that mechanical fields are described by the sum of terms of a third order polynomial function, as for any simple, end-loading beam bending problem, and a series of exponential functions which reflect the smooth transition between the various zones of the specimen due to the compliance of the adhesive layer. From the experimental standpoint, it is important to note the various, process zone characteristic 'wave numbers' which control stress distribution in the adhesive layer. These are:

$$\lambda_\tau = \sqrt{\frac{2wG_a}{t_a}\left(\left(\frac{t}{2}\right)^2\frac{1}{EI} + \frac{1}{ES}\right)} \tag{13}$$

$$\lambda_{\sigma i} = \lambda\sqrt{2(\mu \pm \sqrt{\mu^2 - 1})} \tag{14}$$

where

$$\lambda = \frac{\sqrt{2}}{2}\left(2w\frac{E_a^*}{t_a}\frac{1}{EI}\right)^{1/4} \tag{15}$$

$$\mu = \frac{\sqrt{2w\frac{E_a^*}{t_a}EI}}{\kappa GS} \tag{16}$$

Reciprocals of Eqs. (13) and (14) give the extent of, respectively, mode II and I process zones, and are obtainable using the strain gauge methodology proposed.

Finally, the longitudinal strains of the substrate skin are the quantities measured with the strain gauge instrumentation technique. Strain is related to the local bending moment and normal force according to the relation:

$$\varepsilon_{li} = \frac{N_i}{ES} - s\frac{M_i}{EI}\frac{t}{2} = \frac{du_i}{dx} - s\frac{d\varphi_i}{dx}\frac{t}{2} \tag{17}$$

By taking into account the effect of the interface compliance, an estimate of the energy release rate is given by the relation:

$$G_{II} \approx \frac{9a^2P^2}{16Eb^2h^3}\left[\frac{1}{\lambda_\tau a} + 1\right]^2 \tag{18}$$

Note, that the mode II energy release rate, G_{II}, is directly related to the extent of the process zone, λ_τ^{-1} and crack length a, thus, contrary to classic corrected beam theory, correction is not constant.

4. Results, analysis and discussion

4.1. Static-load transfer

In Fig. 2, the outer skin strain distribution for a unit applied force at the mid-span of the ENF sample is depicted.

Two dummy points are added, corresponding to the edge of the sample ($x = 0$, $x = 180$ mm) were the bending moment and associated longitudinal strain are known to be 0. The sign of the signal depends on whether the gauge is on the compressed (–) or on the elongated (+) side of the sample. In the free, or 'cracked', zone ($x < 44$ mm, no bonding) a linear strain variation is found. Similar linear evolution, but with a different slope (about half that observed in the free zone), is observable in the bonded part of the specimen ($90 < x < 180$ mm), which behaves like a two layer laminate with an elastic interface. The most interesting finding is in the vicinity of the crack tip ($a < x < 90$ mm), where a smooth accommodation phenomenon is clearly visible, associated to a clear decay of the measured strain. This effect was expected since it is related to the load transfer mechanism through the adhesive layer, whose shear stress distribution is controlled by the parameter λ_τ (Eq. (13)).

Since the strain distribution was measured on both sides (tension–compression) of the specimen, complementary calculations are possible. In particular, we wish to assess the (anti)symmetry of specimen deformation, which is a common assumption of ENF associated to pure mode II loading. In the case of 'true' symmetry, the strain measured on the top and bottom sides of the specimen should be equal and of the same sign, as in the DCB cleavage test (*viz.* both exposed adherend skins are in compression). In the ENF, antisymmetric loading is generally assumed: strains are of the same absolute values but of opposite signs (*viz.* tension/compression). The difference between the adherends skin strain values is:

$$\varepsilon_{II} = \Delta\varepsilon_{li} = \frac{1}{2}\left(\frac{t}{2}\frac{\Sigma' M_i}{EI} + \frac{\Delta' N_i}{ES}\right) \tag{19}$$

and allows for evaluation of the mode II contribution. Equivalently, by calculating the sum:

$$\varepsilon_I = \Sigma\varepsilon_{li} = \frac{1}{2}\left(\frac{t}{2}\frac{\Delta' M_i}{EI} + \frac{\Sigma' N_i}{ES}\right) \tag{20}$$

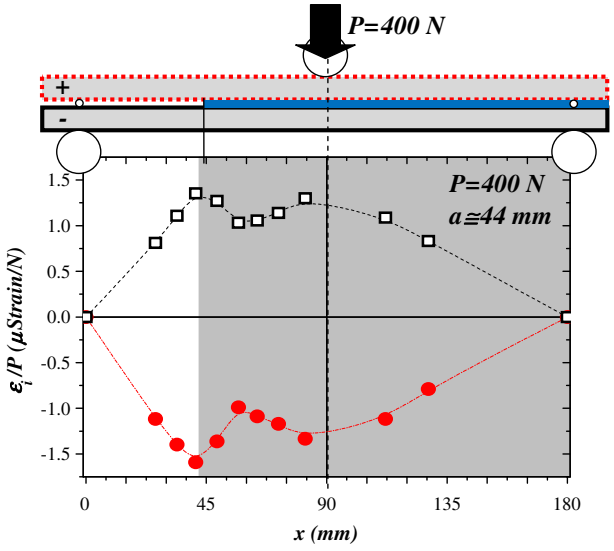

Fig. 2. Comparison between analytical and experimental results. Longitudinal strain as a function of position along the joint.

a simple estimate of the mode I contribution is obtained. Symbols Δ' and $\sum'$, represent the difference and the sum of appropriate load components on both side of the specimen. In relations (19) and (20), indices *s* and *i* correspond to superior (compression) and inferior (tensile) sides of the specimen respectively. These equations are valid, for all possible test configurations on DCB-like specimens, including the standard mode I DCB test, where possible evidence of asymmetry of the bonded plates may be obtained. Such definitions of the fracture mode components (Eqs. (19) and (20)) may be of great importance for joints under mixed mode conditions. Computed and measured ε_I and ε_{II} strain distribution along the sample are presented in Fig. 3, showing good agreement between the two approaches.

Interestingly, in this representation experimental results clearly show a significant mode I load contribution at the crack front in supposedly pure mode II test. Negative opening stress is present, leading to a crack closure mechanism. In the present configuration, where the crack is relatively short (but still *ca.* 0.5*L*), the mode I contribution is *ca.* 15% of that of mode II, which is far from being negligible and might explain the unstable crack propagation when cracks are short (Carlsson et al., 1986). Finally, it should be noticed that mode I strain evolution is identical to that observed previously in the SCB mode I experiments (Budzik et al., 2011a), which corroborates the possibility of decoupling mode I and II contributions using relations (19) and (20). The origin of this "mode I", will be discussed below. More important, at this stage, is to emphasise that mode II is at the heart of present contribution.

4.2. Fracture-analysis of global parameters

In Fig. 4 are presented typical experimental data from the 'fracture' ENF test. Force, *P*, and equivalent effective crack length, a_{eff}, are shown *vs* deflection, δ.

Three different periods can be distinguished: initial loading, crack propagation and crack arrest. The onset of failure is associated with a threshold (δ = *ca.* 0.75 mm, *P* = *ca.* 660 N), so that up to this time the force/deflection curve is (quasi)linear and no crack propagation can be observed. Linear regression was performed on the results, revealing that the compliance of the bonded system was equal to 912^{-1} (mm/N). An intercept was also found, whose

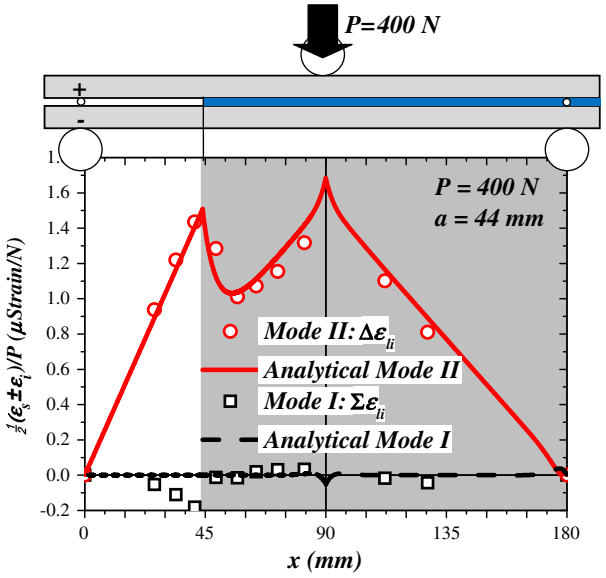

Fig. 3. Comparison between analytical and experimental results. Longitudinal strain as a function of position along the joint.

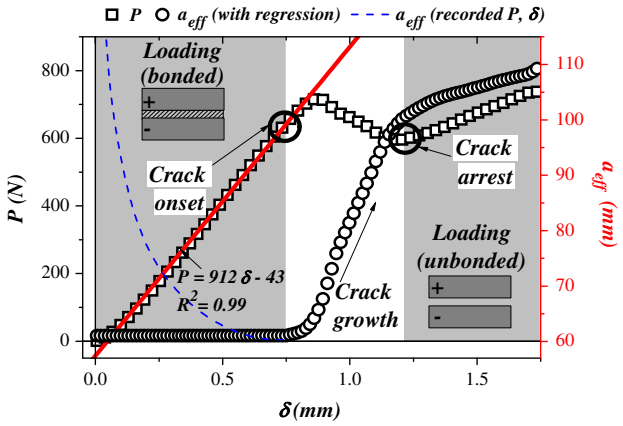

Fig. 4. ENF test results with load, *P*, and effective crack length, a_{eff}, plotted against the load point displacement, δ.

meaning can be understood by the treatment proposed by Blackman et al. (2005), resulting in a corrected crack length. In the present case, the value of this offset (*ca.* 0.05 mm) can probably be attributed to tensile machine elasticity and/or eventually to technological data such as surface roughness. Following this stage, the decrease of load corresponds to stable crack propagation. When the crack approaches the mid-span position, the middle punch hinders crack propagation and the load increases again. With the joint now being partially debonded, the compliance of such a system is three times lower ($=304^{-1}$ mm/N) than when bonded ($=912^{-1}$ mm/N). This suggests that the initial compliance (of the bonded system) scales with $(2t)^3$, while for the cracked system it scales with $2(t + t_a/2)^3$. The evolution of a_{eff} also exhibits the same three periods. During the loading period, after allowing for specimen compliance, a_{eff} remains constant (*const. C*). When $da_{eff}/d\delta$ ($\equiv da_{eff}/dt$) becomes positive, crack growth has started. For comparison, we have represented evolution of a_{eff} as obtained from the 'original' *P* and δ data, without linear regression in the initial stage (as ----). Since the offset value is not allowed for, after crack initiation both curves are exactly the same (the symbols ○ obscure ---- in Fig. 4). However, in the initial, loading stage, differences are marked. The *effective* crack length (----) rapidly decreases and crack onset can be selected as the local minimum of the $a_{eff}(\delta)$ function. The form of the curve may be thought unusual in its original form, nevertheless specimen compliance is low compared to, for instance, thin composite specimens. Being aware of this, we prefer to leave the data as they are, without correction for offset or crack length, since gauge methodology leads directly to these data. We note that if the 'classic' compliance correction is made, crack length will be reduced by 16% in the present case. Accordingly, the 'end' of the propagation period is marked by a change of *apparent* crack growth rate. The transition between crack growth and crack 'arrest' (or, at least, exceedingly slow growth rate) periods is smooth, suggesting that when the crack front approaches the loading pin, increased compressive stress modifies the propagation. Note, that this common belief is not necessarily true. The crack continues to propagate in a stable way after passing the loading point position, following a rise of the applied couple.

In Fig. 5, two images show the bondline both prior to (Fig. 5a) and following (Fig. 5b) passage of the crack over the observed zone. The marks clearly evidence the relative horizontal displacement of the two separated surfaces due to shear. Adhesive (interfacial) failure is noted.

Since the adhesive is not exactly equally shared between both adherends, in the cracked region of the specimen, the apparent bending rigidity of the adherends is likely to be different. This in turn can lead to an asymmetric load distribution between upper

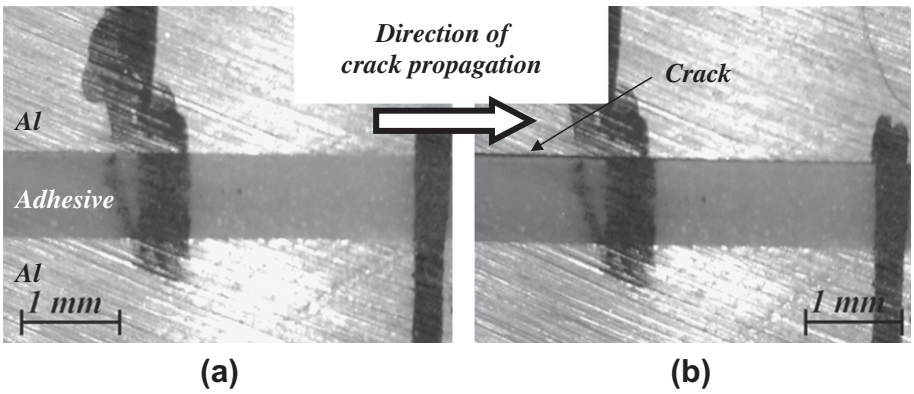

Fig. 5. Crack front propagation in the ENF test. (a) Initial, uncracked state and (b) after crack propagation.

and lower adherends. Indeed, the important thickness of the adhesive layer, combined with the high rigidity of the adhesive itself, will modify flexural rigidity. The flexural rigidity of such a coated beam can be evaluated from the relation (Nicu and Bergaud, 1999):

$$\widetilde{EI} = \frac{w[E^2t^4 + E_a^2t_a^4 + EE_att_a(4t^2 + 6tt_a + 4t_a^2)]}{12(Et + E_at_a)} \tag{21}$$

This effect is generally not taken into account, even if in some experiments adhesive (*i.e.* interfacial) failure is observed. In the present case, the adhesive coating produces *ca.* 5% increase of the beam rigidity. According to the model proposed in part I of this work, this is of almost no importance when treating mode II data, but is crucial when considering the symmetric, mode I contribution.

Finally, traditional data reduction is effected to generate fracture energy *vs.* crack length, also known as the *R*-curve. For a more complete presentation of the experimental results, it is preferable to plot the energy release rate as a function of both crack length and crack speed, which enables us to see any possible viscous effects. The present experimental results are reported in Fig. 6, the fracture energy being estimated from Eq. (2) using a_{eff} as the value of crack length.

During most of the experiment, constant crack propagation rate was found (*ca.* 0.1 mm/s). As propagation advanced, the energy release rate (fracture energy) increased from *ca.* 130 J m^{-2} to *ca.* 275 J m^{-2}. This important variation is difficult to explain at present and we will return to this later on.

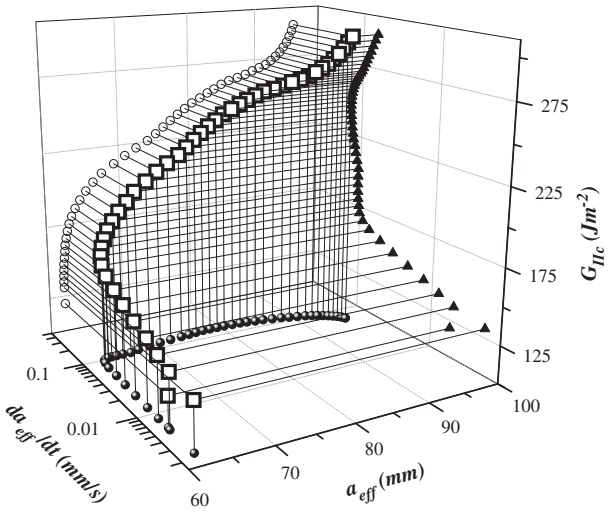

Fig. 6. Fracture energy *vs.* crack speed and crack position as found from global displacement–force relations.

4.3. Local measurements with instrumented ENF test

In the backface strain monitoring technique, strain gauges are bonded to the adherends to measure the longitudinal strain or, equivalently, the local bending moment. In Fig. 7 we present the evolution of measured strain as a function of beam deflection.

Ten curves are presented, corresponding to five measuring positions on each of the specimen's top and bottom sides. The adherend thickness was chosen so that no plastic strain should occur during the test, which is confirmed by the linear strain *vs.* deflection evolution. Furthermore, no irreversible deformation is measured once the sample has been unloaded. However, in the interval $0.7 < \delta < 1.3$ mm, which also corresponds to the crack propagation period, some 'events' are clearly visible on the strain signals. These strain fluctuations correspond to the crack front passing in the vicinity of each gauge position. The analysis presented hereafter indicates that the gauges bonded at position $x = 52$ mm were above the process zone at the beginning of the test. Therefore, we concentrate on the analysis of signal evolution from the eight remaining gauges.

As seen in Fig. 3, the longitudinal strain evolution along the outer side of the adherends clearly exhibits features allowing identification of bondline properties and localisation of the crack front position. Since, the strain gauges are fixed, the only 'distance', or 'position', which grows monotonically during the test is the crack length. As proposed in other configurations (Budzik et al., 2011a,b), the time scale (or equivalently displacement, as in the present case where constant separation rate loading is used) is replaced by the apparent crack length scale obtained from relation (1). Theoretically, the exact geometrical crack tip position could be determined using the analytical correction coefficients, provided the interface compliance is known (Wang and Williams, 1992). In practice, it is easier to construct a correction curve from experimental data directly. As seen in Fig. 3, mode II strain is locally maximal in the vicinity of the crack tip. When a local strain maximum is detected on one of the strain channels, the instantaneous crack tip position is known and corresponds to the position of the strain gauge. In Fig. 8 is shown the correction curve a *vs.* a_{eff} constructed with this method during crack propagation. Four points correspond to gauge measurements, the last point corresponds to the crack arrest position (*viz.* mid-span: $a = 90$ mm).

Since only discrete values of a are obtained with this technique, the correction curve is obtained by interpolation (and eventually extrapolation). From a practical standpoint, in the range $60 \text{ mm} < a < 90$ mm, a simple linear relation is found between

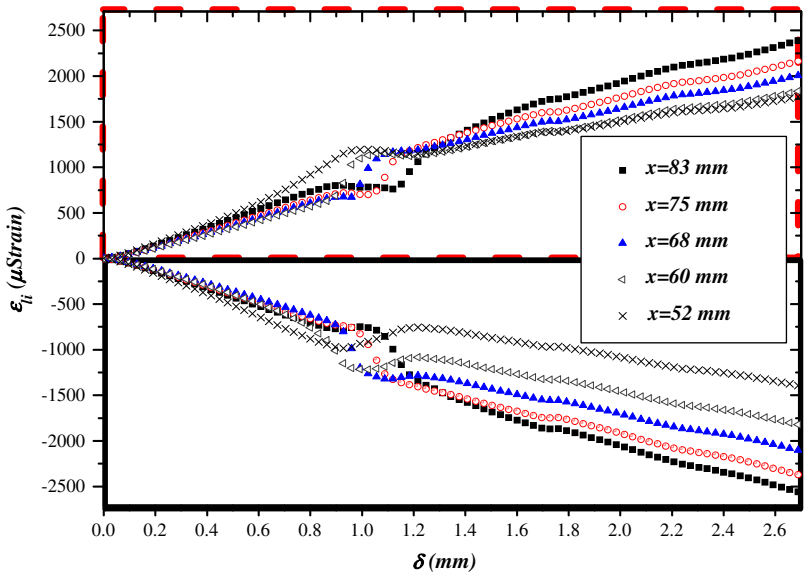

Fig. 7. Raw results from strain gauge measurements: backface strain, ε, *vs.* beam deflection, δ.

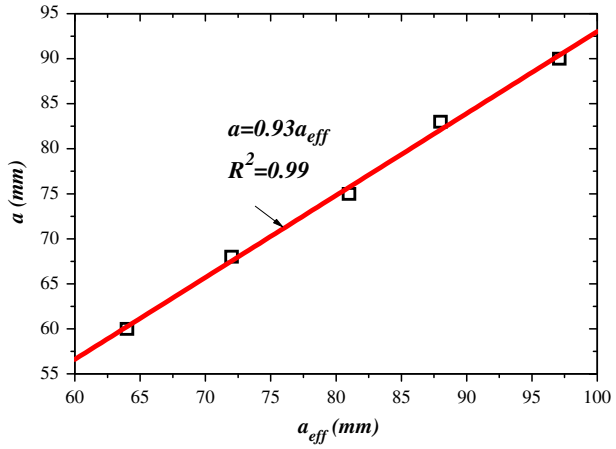

Fig. 8. Relation between real, experimental crack length, a, and its effective estimation, a_{eff}, as obtained from Eq. (1).

the effective and real crack positions ($R^2 = 0.99$). As expected, due to the interface compliance effect, an overestimation of the crack length is found when using the simple beam theory approximation. However, the 'real' a is only *ca.* 7% shorter than the effective value while, as we have noted, the classic compliance correction would provide a reduction of 16%.

Apart from the crack propagation aspect, the specimen is assumed to behave in a linear, elastic manner and the local strain is proportional to the local bending moment, Px, so that all measured strains may be normalised by this value. Additionally, according to simple beam theory, the local strain is inversely proportional to the second moment of the beam cross section, which is different depending on whether the strain is detected above a bonded or cracked region. Then, according to simple beam theory, a step should be observed in the normalised strain evolution when the crack tip meets the strain gauge position, following the relations:

$$\frac{\varepsilon_{free}}{Px} = \frac{t}{8EI} \quad \frac{\varepsilon_{bonded}}{Px} = \frac{t}{16EI} \tag{22}$$

The SBT model indicates a normalised strain value twice as big as that measured in the bonded zone [0.017 μStrain/Nmm] when the crack has passed the gauge position [0.034 μStrain/Nmm].

In Fig. 9 are reported the normalised mode II strains as a function of instantaneous geometrical crack tip position, which are used for quantitative evaluation of the cohesive force distribution along the process zone.

Experimental data are in good agreement with this prediction, showing stationary values when the crack tip is far from the gauges. However, smooth variation is observed, rather than a step, which is consistent with the prediction of our elastic model and outlines the effects of cohesive forces in the process zone. Indeed, the smooth transition between the stationary strain values in bonded and separated regions is well described by a simple elastic model of the ENF specimen. With this model, the estimated value of λ_τ^{-1} is 5.5 mm, corresponding to a shear modulus value of $G_a = 1.5$ GPa. Some disparities are observed between measurements and theoretical predictions which should be appreciated since they offer new possibilities for fine investigation of the adhesive behaviour in the highly stressed region (*viz.* crack tip vicinity). Additionally, it is likely that the friction of the crack 'lips' (relative movement of substrates in the separated zone) should be taken into account in the local modelling of shear cohesive force. Also, an adhesion component may possibly be involved following the

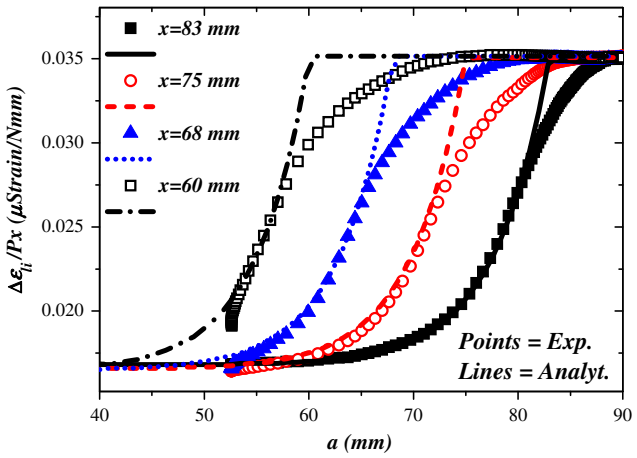

Fig. 9. Distribution of average gauge signals (mode II strain) as a function of crack position. Points correspond to experimental data, lines to analytical solution.

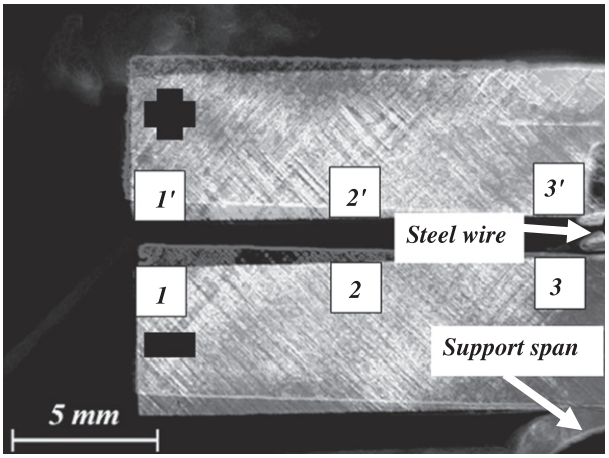

Fig. 10. Initial and final positions of the free edges of the substrates.

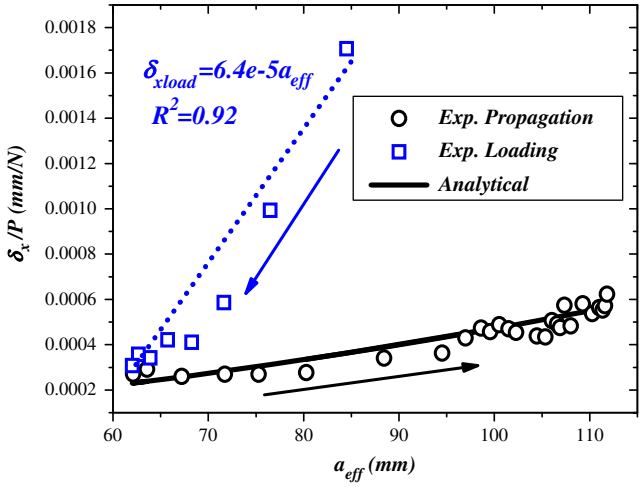

Fig. 11. Shear compliance *vs.* effective crack length.

DMT treatment (Derjaguin et al., 1975). Even if these effects are not visible at a macroscopic scale, some possible evidence is observed here from strain gauge measurements, with the smooth transition between the process zone and the truly cracked part.

4.4. Shear displacement

From direct camera observation and subsequent image analysis (DIC), longitudinal (δ_x) and normal (δ_z) relative displacement components (difference between upper and lower substrate displacements) were obtained. Initial and deformed configurations are depicted in Fig. 10. Displacement components were estimated from relative positions of the beam corners, corresponding to contact with the adhesive (therefore exactly at the expected contact line).

In Fig. 11, the experimental shear compliance (δ_x/P) is plotted *vs.* effective crack length, together with the analytical solution obtained from:

$$\delta_x = \left[\frac{t}{2}\varphi(x=0)\right]_+ + \left[\frac{t}{2}\varphi(x=0)\right]_- \tag{23}$$

The effective crack length representation is preferred here since the initial decrease in the compliance with decreasing crack length (displacement increase is indicated with arrows in Fig. 11) is indeed virtual, corresponding to the crack onset period, without propagation. We note that crack onset can be easily obtained from such a compliance curve, corresponding to the (sharp) inflection point. An important change in the sample compliance gives a figure to differences between the two stages: loading and crack propagation. Experimental results of shear compliance could be used to estimate mode II energy release rate using (Kageyama et al., 1992):

$$G_{II} = \frac{3P^2}{8wt}\left(\frac{\delta_x}{P}\right) \tag{24}$$

The results obtained with this estimate are represented as *R*-curves in Fig. 12 together with simple beam theory results [*viz.* Eq. (2), where effective and real values of crack lengths were used] and the present model using the process zone description, Eq. (18).

Good agreement is found between the various estimates. Despite using the uncorrected effective crack length in Eq. (2), results are in excellent agreement with the model postulated, where the proposed correction takes into account both the adherend effect and interface compliance effects. The crack length, as estimated by the uncorrected SBT model (*effective* crack length) compensates the effect of adhesive deformation. Similar behaviour was observed in the single cantilever beam test under mode I loading (Budzik et al., 2011c). All the methods developed for the evaluation of crack length and energy release rate indicate similar results and show an increase of the fracture energy with crack

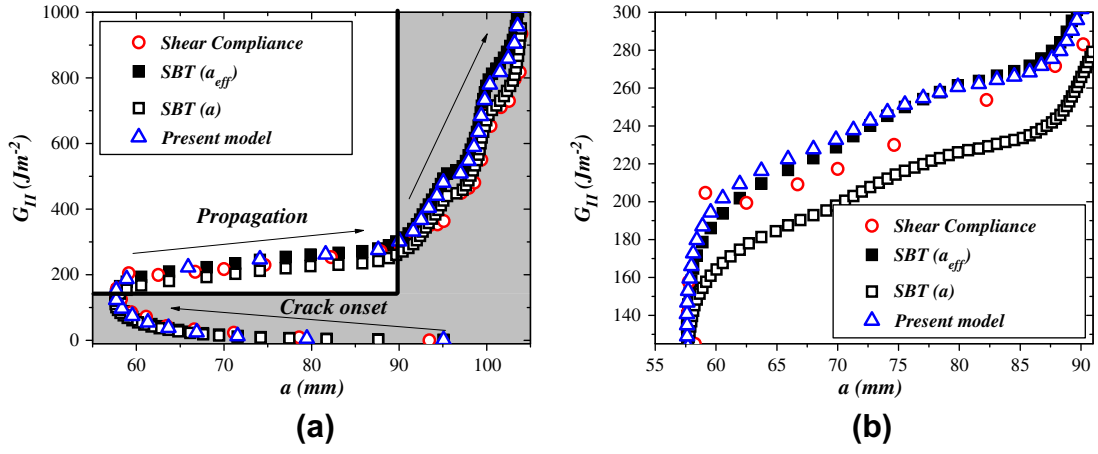

Fig. 12. Estimates of mode II energy release rate from simple beam theory, Eq. (2) with uncorrected and corrected crack length and shear compliance, Eq. (24). (a) Effective *R*-curves for all models. (b) Zoom on crack propagation period.

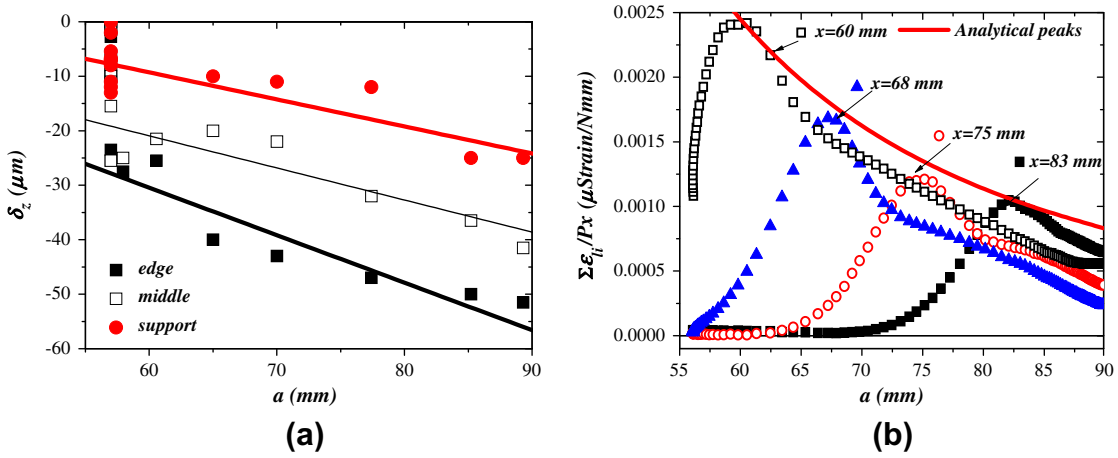

Fig. 13. (a) Results of DIC analysis: vertical gap between upper and lower adherends *vs.* crack front position. (b) Distribution of the difference in gauge signals (mode I strain) as a function of crack position. Points correspond to experimental data, lines to analytical solution.

length (Fig. 12b), which is consistent with others findings (Yoshihara, 2003, 2004, 2005; de Moura et al., 2009).

4.5. Mode I contribution

In Fig. 13a, the difference between upper and lower vertical components of the free beam edge (see Fig. 10) displacement, δ_z, is plotted *vs.* effective crack length. Three positions, *cf.* Fig. 10, are considered. 1,1′ – edge (corner) of the 'free beam', 2,2′ – middle position between support span line and free corner and 3,3′ – approximate support position, which corresponds to a distance of *ca.* 0.5 mm from the support span line (which was not recorded in its entirety). Results prove a lever effect, associated with finite bondline compressive rigidity, as discussed in part I of this work. A quasilinear decrease of the gap at all three positions is found. Linear evolution *vs.* position along the beam can also be obtained (although not presented here). We report that our method is able to filter such an effect. In Fig. 13b, results of application of Eq. (20) to the gauge signals are presented. As previously, data are normalised by the applied bending moment (Px).

Analytical results, in the form of mode I peak values (*NB.* when gauge position = crack position), stay in very good agreement when considering the imperfect boundary conditions and adhesive failure (Fig. 5). The mode I contribution amplitude decreases monotonically during propagation. Also, a characteristic shape is retained. Moreover, results are consistent with those from DIC. Soft contact, and a gap between spacer and adherend explain the development of a compressive stress causing crack closure near the crack tip, which may delay the crack onset.

Overall, it can be seen that crack front phenomena are exceedingly complex. Although not all aspects (*cf.* part I) have been covered here, we believe this to be the most detailed description to date. Strain gauge instrumentation demonstrates its value for fine and continuous investigation of cohesive force evolution in the vicinity of the crack tip. With this technique, precise evaluation of the energy release rate can be effected and more importantly, accurate assessment of test conditions (mode mixity, friction effect) is obtained.

5. Conclusions

We have proposed a strain gauge instrumentation technique for the three point bending end notched flexure (ENF) mode II adhesive test. This technique, converting bonded substrates into 'load cells', allows evaluation of cohesive force distribution in the vicinity of the crack front. Two configurations have been studied: (a) static, in which the test piece was loaded without damaging the bondline and (b) fracture, with the crack continuously growing. Results obtained with strain gauge instrumentation were compared with more standard analysis. From the experiments realised we draw the following major conclusions:

- Instrumentation of the ENF test piece with strain gauges gives considerable insight into process zone phenomena. Crack onset and process zone are identified from strain gauge data. This method being both precise and reliable, could be particularly useful for validation and verification of analytical and finite element models, including those of the cohesive zone.
- Strain gauge results indicate that mode II/I mixity can be present at the crack front. Not expected, however, was crack closure. Mode I decreases with increasing crack length. For correct estimation of the mode II fracture energy, long cracks are advised. The mode I component and thus any eventual mode mixity can be quantified using the method proposed.
- We found the Timoshenko beam on a Pasternak two-parameter elastic foundation approach fruitful in interpreting process zone behaviour. This model provides a correct phenomenological description of the experimental findings *viz.* process zone characteristic number, λ_τ.
- As expected, simple beam theory (SBT) overestimates real crack length. This latter can be successfully corrected by studying gauge signal history. In the present case, we found that SBT overestimates the crack position by *ca.* 7%. This ratio is constant during crack propagation. A correction could be used to evaluate the mode II energy release rate *viz.* using corrected beam theory.
- Shear compliance was successfully obtained using the digital image correlation technique.
- Similar values of the energy release rate were found with the SBT model using the effective (uncorrected) crack length, uncorrected shear compliance and the presently postulated model taking into account process zone phenomena. Values of fracture energy found are $G_{II} \approx 130 \rightarrow 275\ \mathrm{J\,m^{-2}}$ depending on crack speed and/or crack length.

As a perspective, we consider that the strain gauge monitoring technique could be used to determine precise values of stresses at the front of a moving crack, as well as in the process zone. This method could be used for practically any structural bonded system.

References

Alfano, G., 2006. On the influence of the shape of the interface law on the application of cohesive-zone models. Comput. Sci. Technol. 66, 723–730.

Alfredsson, K.S., 2004. On the instantaneous energy release rate of the end-notch flexure adhesive joint specimen. Int. J. Solids Struct. 41 (16–17), 4787–4807.

Banea, M.D., da Silva, L.F.M., 2009. Adhesively bonded joints in composite materials: an overview. Proc. Inst. Mech. Engrs. Part L: J. Mater. Des. Appl. 223, 1–18.

Barrett, J.D., Foschi, R.O., 1977. Mode II stress–intensity factors for cracked wood beams. Eng. Fract. Mech. 9 (2), 371–378.

Bennati, S., Colleluori, M., Corigliano, D., Valvo, P.S., 2009. An enhanced beam-theory model of the asymmetric double cantilever beam (ADCB) test for composite laminates. Comput. Sci. Technol. 69, 1735–1745.

Blackman, B.R.K., Kinloch, A.J., Paraschi, M., 2005. The determination of the mode II adhesive fracture resistance, G_{IIc}, of structural adhesive joints: an effective crack length approach. Eng. Fract. Mech. 72, 877–897.

Budzik, M.K., Jumel, J., Shanahan, M.E.R., 2011a. An *in situ* technique for the assessment of adhesive properties of a joint under load. Int. J. Fract. 171 (2), 111–124.

Budzik, M.K., Jumel, J., Shanahan, M.E.R., 2011b. Process zone in the single cantilever beam under transverse loading – Part II: Experimental. Theor. Appl. Fract. Mech. 56 (1), 13–21.

Budzik, M.K., Jumel, J., Shanahan, M.E.R., 2011c. Effect of adhesive compliance in the assessment of soft adhesives with the wedge test. J. Adhes. Sci. Technol. 25 (1–3), 131–149.

Carlsson, L.A., Gillespie Jr., J.W., Pipes, R.B., 1986. On the analysis and design of end notched flexure (ENF) for mode II testing. J. Compos. Mater. 20, 594–604.

Chai, H., Mall, S., 1988. Design aspects of the end-notch adhesive joint specimen. Int. J. Fract. 36 (1), R3–R8.

Corleto, C.R., Hogan, H.A., 1995. Energy release rates for the ENF specimen using a beam on an elastic foundation. J. Compos. Mater. 29 (11), 1420–1436.

Davidson, B.D., Sun, X., 2006. Geometry and data reduction recommendations for a standardized end notched flexure test for unidirectional composites. J. ASTM Int. 3 (9), 1–19.

Derjaguin, B.V., Muller, V.M., Toporov, Y.P., 1975. Effect of contact deformations on adhesion of particles. J. Colloid Interf. Sci. 53 (2), 314–326.

D2919-01, 2007. Standard Test Method for Determining Durability of Adhesive Joints Stressed in Shear by Tension Loading.

D3165-07 Standard Test Method for Strength Properties of Adhesives in Shear by Tension Loading of Single-Lap-Joint Laminated Assemblies.

D3166-99, 2005. Standard Test Method for Fatigue Properties of Adhesives in Shear by Tension Loading (Metal/Metal).

D3433-99, 2005. Standard Test Method for Fracture Strength in Cleavage of Adhesives in Bonded Metal Joints.

D3762-03 Standard Test Method for Adhesive-Bonded Surface Durability of Aluminium (Wedge Test).

de Moura, M.F.S.F., Campilho, R.D.S.G., Gonçalves, J.P.M., 2009. Pure mode II fracture characterization of composite bonded joints. Int. J. Solids Struct. 46 (6), 1589–1595.

Erdogan, F., 1965. Stress distribution in bonded dissimilar materials with cracks. J. Appl. Mech. 32, 403–410.

Goland, M., Reissner, E., 1944. The stresses in cemented joints. J. Appl. Mech. Trans. ASME 11, A17–A27.

He, M.Y., Hutchinson, J.W., 1989. Crack deflection at an interface between dissimilar elastic materials. Int. J. Solids Struct. 25, 1053–1067.

Jumel, J., Budzik, M.K., Shanahan, M.E.R., 2011. Process zone in the single cantilever beam under transverse loading – Part I: Theoretical analysis. Theor. Appl. Fract. Mech. 56 (1), 7–12.

Jumel, J., Budzik, M.K., Ben Salem, N., Shanahan, M.E.R., 2012. Part I of Present Contribution.

Kageyama, K., Kikuchi, M., Yanagisawa, N., 1992. Stabilized end notched flexure test. Characterization of mode II interlaminar crack growth. ASTM STP 1110, 210–225.

Kendall, K., 1975. Crack propagation in lap shear joints. J. Phys. D Appl. Phys. 8 (5), 512–522.

Kuczmaszewski, J., 2006. Fundamentals of Metal–Metal Adhesive Joint Design. Lublin University of Technology, Polish Academy of Sciences, Lublin Branch, Lublin.

Leffler, K., Alfredsson, K.S., Stigh, U., 2007. Shear behaviour of adhesive layers. Int. J. Struct. Solids 44, 530–545.

Leguillon, D., 2002. Strength or toughness? A criterion for crack onset at a notch. Eur. J. Mech. A/Solids 21 (1), 61–72.

Mall, S., Kochar, N.K., 1986. Finite Element Analysis of End Notch Flexure Specimen. NASA Contractor Report 178113.

Martin, R.H., Davidson, B.D., 1999. Mode II fracture toughness evaluation using a four point bend end notched flexure test. Plast. Rubbers Compos. 28 (8), 401–406.

Mostovoy, S., Crosley, P.B., Ripling, E.J., 1967. Use of crack-line-loaded specimens for measuring plane-strain fracture toughness. J. Mater. 2, 661–668.

Nicu, L., Bergaud, C.J., 1999. Experimental and theoretical investigations on nonlinear resonances of composite buckled microbridges. J. Appl. Phys. 86, 5835.

Ouyang, Z., Li, Q., 2009. Nonlinear interface shear fracture of end notched flexure specimens. Int. J. Solids Struct. 46 (13), 2659–2668.

Russell, A.J., 1982. Factors affecting the interlaminar fracture energy of graphite/tpoxy laminates. In: Progress in Science and Engineering of Composites; Proceedings of ICCM-IV, Tokyo, pp. 279–286.

Reissner, E., 1944. On the theory of bending of elastic plates. J. Math. Phys. 23, 184–191.

Sørensen, B.F., Jacobsen, T.K., 2003. Determination of cohesive laws by the *J* integral approach. Eng. Fract. Mech. 70 (14), 1841–1858.

Tsai, M.Y., Morton, J., 1994. An evaluation of analytical and numerical solutions to the single-lap joint. Int. J. Solids Struct. 31 (18), 2537–2563.

Wang, H., Vu-Khanh, T., 1996. Use of end-loaded-split (ELS) test to study stable fracture behaviour of composites under mode II loading. Comput. Struct. 36 (1–2), 71–79.

Wang, Y., Williams, J.G., 1992. Corrections for mode II fracture toughness specimens of composite materials. Compos. Sci. Technol. 43 (3), 251–256.

WK22949 New Test Method for Determination of the Mode II Interlaminar Fracture Toughness of Unidirectional Fiber-Reinforced Polymer Matrix Composites Using the End-Notched Flexure (ENF) Test.

Yoshihara, H., 2003. Resistance curve for the mode II fracture toughness of wood obtained by the end-notched flexure test under the constant loading point displacement condition. J. Wood. Sci. 49 (3), 210–215.

Yoshihara, H., 2004. Mode II *R*-curve of wood measured by 4-ENF test. Eng. Fract. Mech. 71 (13–14), 2065–2077.

Yoshihara, H., 2005. Mode II initiation fracture toughness analysis for wood obtained by 3-ENF test. Comput. Sci. Technol. 65 (14), 2198–2207.

Zhang, Z.H., Shang, J.K., Lawrence, F.V., 1995. A backface strain technique for detecting fatigue crack initiation in adhesive joints. J. Adhesion 49, 23–36.